RSC Advances

PAPER

View Article Online
View Journal | View Issue

Cite this: *RSC Adv.*, 2021, **11**, 3058

Novel structural phases and the properties of LaX (X = P, As) under high pressure: first-principles study

Yu Zhou,[a] Lan-Ting Shi,[a] A-Kun Liang,[b] Zhao-Yi Zeng,*[c] Xiang-Rong Chen*[a] and Hua-Yun Geng[d]

Received 30th October 2020
Accepted 6th January 2021

DOI: 10.1039/d0ra09238j

rsc.li/rsc-advances

The particle swarm optimization algorithm and density functional theory (DFT) are extensively performed to determine the structures, phase transition, mechanical stability, electronic structures, and thermodynamic properties of lanthanide phosphates (LaP and LaAs) in the pressure range of 0 to 100 GPa. Two novel high-pressure structures of LaP and LaAs are first reported here. It is found that LaX (X = P, As) undergo a phase transition from NaCl-type structure (*Fm*3*m*) to CsCl-type structure (*P*4/*mmm*) at 19.04 GPa and 17.22 GPa, respectively. With the elevation of the pressure, *C*2/*m*-LaP and *Imma*-LaAs are the most stable structures up to 70.08 GPa and 85.53 GPa, respectively. Finally, the analysis of the elastic constants and hardness confirms that the *C*2/*m*-LaP possesses hardness values up to 23.24 GPa due to the strong covalent P–P bonding and ionic La–P bonding, indicating that it is a potential hard material.

1. Introduction

Rare-earth (RE) monopnictides have attracted extensive attention due to their excellent properties of high melting point, extreme magnetoresistance, and high superconductivity. These properties make them widely applied in many fields, such as sensors, spintronics, infrared (IR) detectors, and magnetic storage devices.[1–11] As the first member of the rare earth monopnictides family, it is very important to understand lanthanum monopnictides in order to look for more interesting properties of this family. In the past decades, a series of studies have been carried out on the fundamental properties of lanthanum pnictides (including electronic, elastic, optical and mechanical properties). For example, Charifi *et al.*[12] and Shoaib *et al.*[9] used full-potential linearized augmented plane wave (FP-LAPW) calculations on the electronic structures of lanthanum pnictides. Vaitheeswaran *et al.*[13] studied the structural and electronic properties of lanthanum pnictides by means of the self-consistent tight binding linear muffin tin orbital (TB-LMTO) method. In addition, Kwon *et al.*[14] measured the optical properties of these compounds. Tütüncü *et al.*[15] determined the elastic properties of these compounds using ultrasonic measurement techniques and through experimental phonon spectroscopy.

High pressure is an effective tool to discover new phenomena and explore new materials. Presently, there are some reports on the structural phase transition and electronic properties of LaX (X = P, As) under high pressure.[12,16–19] At ambient conditions, LaX (X = P, As) are cubic structures of NaCl type (B1 phase) with space group of *Fm*3*m*. Under lower pressure, they undergo a structure phase transition into a tetragonal distorted structure of CsCl type (PT phase) with a space group of *P*4/*mmm*. In theory, Charifi *et al.*[12] showed that LaX (X = P, As) transformed from cubic structure to tetragonal structure in the range of 14.6 to 22.6 GPa for LaP and 11.2 to 19.6 GPa for LaAs, respectively. Vaitheeswaran *et al.*[20] investigated the electronic structure and the relative stability of LaP and LaAs at high pressure. They found that the phase transition from rocksalt to tetragonal occurred around 18 GPa and 11.2 GPa in the case of LaP and LaAs, respectively. In experiments, high-pressure synchrotron X-ray diffraction experiment revealed that the phase transition was found at around 24 GPa for LaP[16] and the pressure-volume relationship extracted from the synchrotron X-ray diffraction pattern showed that the phase transition of LaAs occurred at around 20 GPa.[19] Similar transformations have also been observed in other rare earth family members, such as PrAs,[21] NdAs,[21] SmAs,[21] and PrSb.[22] Recently, Khalid *et al.*[4] found that the hydrostatic pressure can induce the p–d crossing of LaAs, showing a topological phase transition at about 7 GPa. However, there are few studies on lanthanide phosphates LaX (X = P, As) under higher pressures.

The purpose of this work is to study the structural, dynamical, mechanical, thermodynamic properties and electronic structures of lanthanide phosphates LaX (X = P, As) under high pressures. Using CALYPSO method,[23,24] the structures of LaX (X = P, As) are investigated under pressures up to 100 GPa. It is

[a]*College of Physics, Sichuan University, Chengdu 610064, China. E-mail: xrchen@scu.edu.cn*

[b]*Departamento de Física Aplicada-ICMUV-MALTA Consolider Team, Universitat de València, Burjassot (Valencia) 46100, Spain*

[c]*College of Physics and Electronic Engineering, Chongqing Normal University, Chongqing 400047, China. E-mail: zhaoyizeng@126.com*

[d]*National Key Laboratory for Shock Wave and Detonation Physics Research, Institute of Fluid Physics, CAEP, Mianyang 621900, China*

found that the *Fm*3*m*-LaX (X = P, As) phases undergo structural phase transitions to *P*4/*mmm*-LaX (X = P, As) phases at lower pressure (19.04 GPa and 17.22 GPa). Moreover, two novel structural phases *C*2/*m*-LaP and *Imma*-LaAs have been proved to be the most stable structures under higher pressures.

2. Computation details

We search for the high-pressure structures of LaP and LaAs using the global structural optimization CALYPSO code with the particle-swarm optimization (PSO) algorithm,[23,24] which is not affected by any prior known structure information and has successfully predicted the high-pressure structures of different systems.[25–28] The calculations of structural relaxations, total-energy and electronic structure are carried out in the framework of density functional theory (DFT) with the generalized gradient approximation of Perdew–Burke–Ernzerhof (GGA-PBE)[29] exchange-correlation functional with the projector augmented wave (PAW)[30] method as implemented in Vienna *ab initio* simulation package (VASP).[31] The plane-wave kinetic energy cutoff is set up to 800 eV, and the Brillouin zone sampling is performed by using *k*-grids with a spacing of $2\pi \times 0.02$ Å^{-1}. The convergence of the total energy and forces is 1×10^{-6} eV per atom and 0.01 eV Å^{-1}, respectively. The phonon calculations are carried out by applying the real-space supercell approach (finite-displacement) and density function perturbation theory (DFPT)[32] implemented in the PHONOPY[33] program. The figures of crystal structures, atomic displacement patterns and electron localization function (ELF)[34,35] are produced using the VESTA software.

3. Results and discussion

3.1 Phase transition and structural properties

In order to determine the high-pressure crystal structures of LaX (X = P, As), we performed the crystal structures prediction in the pressure range of 0–100 GPa with simulation sizes from one to eight formula units (f.u.) per cell. The results showed that *Fm*3*m*-LaX (X = P, As) (Fig. 1a) are the most stable structures at 0 GPa and *P*4/*mmm*-LaX (X = P, As) (Fig. 1b) become the most stable structures at 50 GPa, consistent with the previous results,[9,12,19,20,36,37] showing the reliability of our research. At the higher pressure of 100 GPa, two novel structures (*C*2/*m*-LaP and *Imma*-LaAs) are predicted, as shown in (Fig. 1c and d). The structural stability and other properties of them will be studied in the following.

To verify the stable phase at high pressure, the variations of enthalpy differences of LaP and LaAs with pressures are presented in Fig. 2. The relationships between volume and pressure are shown in Fig. 3. Our results show that, when the pressure increases, the cubic structures (*Fm*3*m*-LaP/LaAs) will be transformed into tetragonal structures (*P*4/*mmm*-LaP/LaAs). The corresponding phase transition pressures of LaP and LaAs are 19.04 GPa and 17.22 GPa, respectively, with the volume collapse are about 10.2% and 9.8%, which are consistent with other available researches.[19,20,37] In the inset of Fig. 2a and b, the enthalpy differences are additionally presented to show clearly the phase transition at higher pressures. It is found that the lowest enthalpies for LaP and LaAs are different. For LaP, *C*2/*m* has the lowest enthalpy, while for LaAs, the enthalpy of *Imma* is lower than that of *C*2/*m*, so *C*2/*m* is the most stable phase of LaP

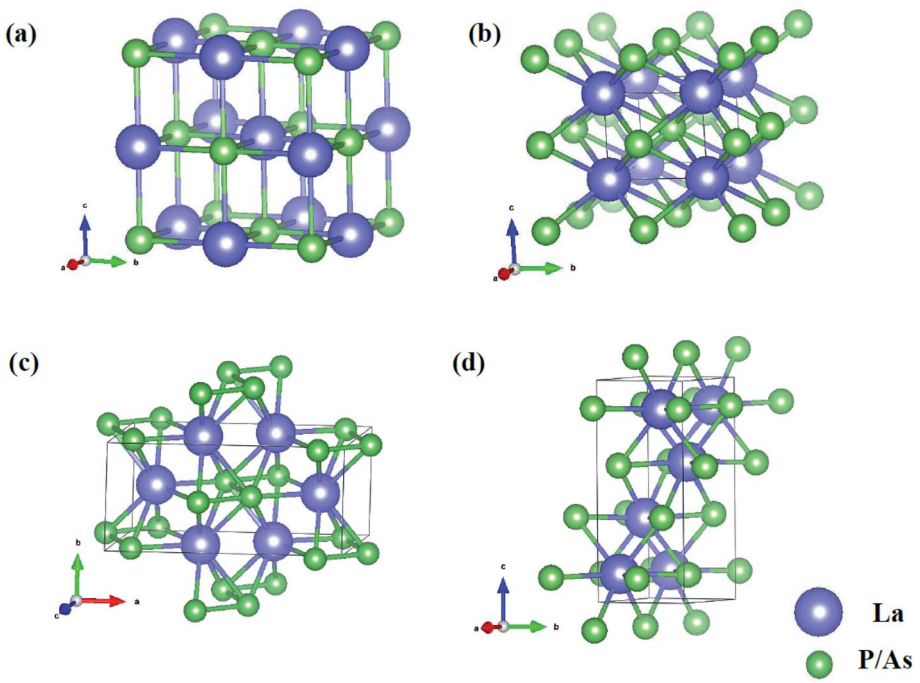

Fig. 1 Crystal structures of (a) *Fm*3*m*-LaX (X = P, As) at 0 GPa; (b) *P*4/*mmm*-LaX (X = P, As) at 50 GPa; (c) *C*2/*m*-LaP at 100 GPa; (d) *Imma*-LaAs at 100 GPa. The purple and green spheres represent the La and P/As atoms, respectively.

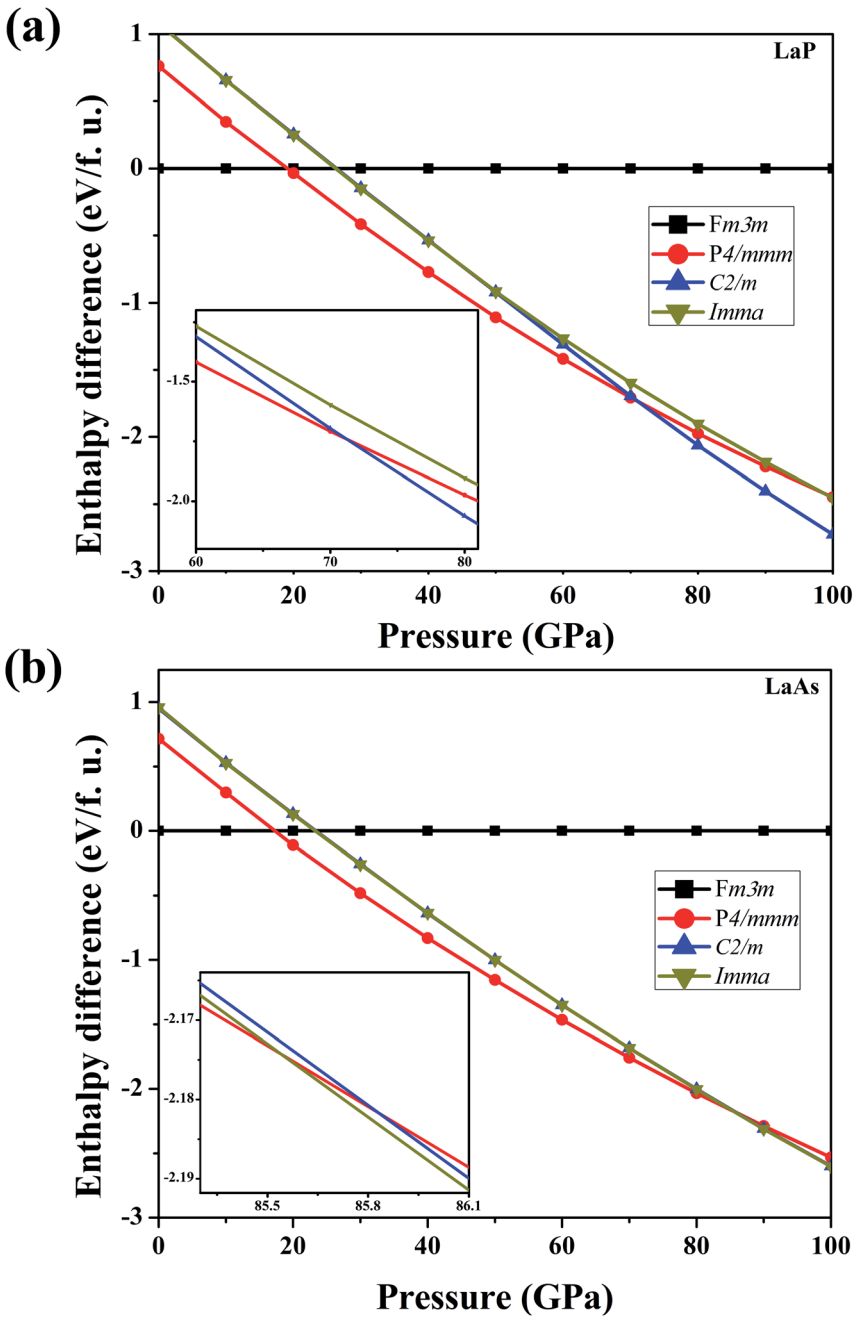

Fig. 2 Calculated enthalpy differences of LaP (a) and LaAs (b) with respect to *Fm3m*-LaX (X = P, As) as functions of pressure range from 0 to 100 GPa. Insets show (a) enthalpy differences of LaP in the range of 60–80 GPa and (b) that of LaAs in the range of 85–86 GPa.

and *Imma* is the stable phase of LaAs at 100 GPa. The corresponding transformation pressures are 70.08 GPa and 85.53 GPa, and the changes in volume collapse are about 3.1% and 1.3%, respectively. Therefore, the sequence of phase transition is *Fm3m* → *P4/mmm* → *C2/m* for LaP and *Fm3m* → *P4/mmm* → *Imma* for LaAs, respectively.

The lattice parameters, atomic coordinates and relative formation enthalpies of the three phases at several pressures are listed in Table 1. The formation enthalpies are defined by $\Delta H = H(\mathrm{LaX}) - H(\mathrm{La}) - H(\mathrm{X})$, where X represents P and As atom, respectively. H is the enthalpy per formula unit of the most stable structure under a given pressure. The discussions of *Fm3m* structures of LaP and LaAs have been mentioned in our previous studies.[38,39] In the *P4/mmm* phase, which contains two atoms per primitive unit-cell, each La atom is surrounded by four P/As atoms. The bond lengths of La–P and La–As are 2.80 and 2.87 Å, respectively. The calculated lattice constants of LaP are $a = 3.507$ Å and $c = 3.004$ Å at 20 GPa, well consistent with the experimental value ($a = 3.460$ Å, $c = 3.007$ Å)[16] and theoretical lattice constants ($a = 3.530$ Å, $c = 3.059$ Å calculated by Vaitheeswaran *et al.*,[20] $a = 3.711$ Å, $c = 3.82$ Å calculated by Charifi *et al.*[12]). The lattice constants of LaAs are $a = 3.684$ Å and

Table 1 Calculated lattice parameters, atomic coordinates and formation enthalpy ΔH(eV per f.u.) of LaX (X = P, As)

LaP	Structures	Pressures	Lattice parameters (Å, deg.)	Atomic coordinates		ΔH
	*Fm*3*m*	0	$a = b = c = 6.050$	La	(0.000, 0.000, 0.000)	−2.026
			$\alpha = \beta = \gamma = 90$	La	(0.000, 0.500, 0.500)	
				La	(0.500, 0.000, 0.500)	
				La	(0.500, 0.500, 0.000)	
				P	(0.500, 0.500, 0.500)	
				P	(0.500, 0.000, 0.000)	
				P	(0.000, 0.500, 0.000)	
				P	(0.000, 0.000, 0.500)	
	*P*4/*mmm*	50	$a = b = 3.407$, $c = 2.892$	La	(0.000, 0.000, 0.500)	−0.863
			$\alpha = \beta = \gamma = 90$	P	(0.500, 0.500, 0.000)	
	*C*2/*m*	100	$a = 4.063$, $b = 3.589$, $c = 8.202$	La	(0.859, 0.500, 0.609)	−0.137
			$\alpha = \beta = 90$, $\gamma = 137$	La	(0.141, 0.500, 0.391)	
				La	(0.358, 0.000, 0.609)	
				La	(0.641, 0.000, 0.391)	
				P	(0.907, 0.000, 0.157)	
				P	(0.093, 0.000, 0.843)	
				P	(0.407, 0.500, 0.157)	
				P	(0.593, 0.500, 0.843)	
LaAs	Structures	Pressures	Lattice parameters (Å, deg.)	Atomic coordinates		ΔH
	*Fm*3*m*	0	$a = b = c = 6.151$	La	(0.500, 0.500, 0.500)	−1.846
			$\alpha = \beta = \gamma = 90$	La	(0.500, 0.000, 0.000)	
				La	(0.000, 0.500, 0.000)	
				La	(0.000, 0.000, 0.500)	
				As	(0.000, 0.000, 0.000)	
				As	(0.000, 0.500, 0.500)	
				As	(0.500, 0.000, 0.500)	
				As	(0.500, 0.500, 0.000)	
	*P*4/*mmm*	50	$a = b = 3.506$, $c = 2.928$	La	(0.000, 0.000, 0.000)	−0.686
			$\alpha = \beta = \gamma = 90$	As	(0.500, 0.500, 0.500)	
	Imma	100	$a = 4.063$, $b = 3.589$, $c = 8.201$	La	(0.000, 0.750, 0.872)	−0.255
			$\alpha = \beta = \gamma = 90$	La	(0.500, 0.750, 0.628)	
				La	(0.500, 0.250, 0.372)	
				La	(0.000, 0.250, 0.128)	
				As	(0.500, 0.250, 0.883)	
				As	(0.000, 0.250, 0.617)	
				As	(0.000, 0.750, 0.383)	
				As	(0.500, 0.750, 0.117)	

c = 3.108 Å at 20 GPa, consistent well with the available experimental data (a = 3.625 Å, c = 3.06 Å)[19] and other theoretical value (a = 3.645 Å, c = 3.171 Å).[20] Upon compression, the *P*4/*mmm*-LaP/LaAs are predicted to be the monoclinic structure *C*2/*m* for LaP and the orthorhombic structure *Imma* for LaAs. For the *C*2/*m*-LaP and *Imma*-LaAs structures, the obtained equilibrium lattice parameters are: $a = 4.063$ Å, $b = 3.589$ Å, $c = 8.202$ Å and $a = 4.063$ Å, $b = 3.589$ Å, $c = 8.201$ Å, respectively. We noticed that there is no experimental and theoretical information on the structural behavior of LaP and LaAs under high pressures. These results are of great significance for further understanding of the high-pressure characteristics of lanthanide phosphates.

3.2 Elastic properties

Through the strain-stress method, we obtained the elastic constants C_{ij} of LaX (X = P, As) at different pressures, which are listed in Table 2. The positive values of the elastic constant matrix of LaAs at different pressures indicate that they are elastically stable. According to the criteria of crystal mechanical stability, if the elastic constants of each phase satisfy the generalized elastic stability criteria, they can be considered mechanically stable.[40] The mechanical stability criteria are as follows:[41]

For $Fm\bar{3}m$ structures:

$$C_{11} > 0,\ C_{44} > 0,\ C_{11} > |C_{12}|,\ C_{11} + 2C_{12} > 0$$

For *P*4/*mmm* structures:

$$C_{11} > |C_{12}|,\ 2C_{13}^2 < C_{33}(C_{11} + C_{12}),\ C_{44} > 0,\ C_{66} > 0$$

For *Imma* structures:

$$C_{11} > 0,\ C_{44} > 0,\ C_{55} > 0,\ C_{66} > 0,\ C_{11}C_{22} > C_{12}^2,\ C_{11}C_{22}C_{33} + 2C_{12}C_{13}C_{23} - C_{11}C_{23}^2 - C_{22}C_{13}^2 - C_{33}C_{12}^2 > 0$$

For *C*2/*m* structures:

$$C_{11} > 0,\ C_{22} > 0,\ C_{33} > 0,\ C_{44} > 0,\ C_{55} > 0,\ C_{66} > 0,\ (C_{22} + C_{33}) - 2C_{23} > 0,\ (C_{33}C_{55} - C_{35}^2) > 0,\ (C_{44}C_{66} - C_{46}^2) > 0,\ C_{11} + C_{22} + C_{33} + 2(C_{12} + C_{13} + C_{23}) > 0,\ C_{22}(C_{33}C_{55} - C_{35}^2) + 2C_{23}C_{25}C_{35} - C_{23}^2C_{55} - C_{25}^2C_{33} > 0,\ 2[C_{15}C_{25}(C_{33}C_{12} - C_{13}C_{23}) + C_{15}C_{35}(C_{22}C_{13} - C_{12}C_{23}) + C_{25}C_{35}(C_{11}C_{23} - C_{12}C_{13})] - [C_{15}^2(C_{22}C_{33} - C_{23}^2) + C_{25}^2(C_{11}C_{33} - C_{13}^2) + C_{35}^2(C_{11}C_{22} - C_{12}^2)] + C_{55}C_{11}C_{22}C_{33} - C_{11}C_{23}^2 - C_{22}C_{13}^2 - C_{33}C_{12}^2 + 2C_{12}C_{13}C_{23} > 0$$

It is found that the calculated elastic constants for LaX (X = P, As) (including *C*2/*m*-LaP) all satisfy the above conditions at pressure, confirming their mechanical stabilities. The calculated elastic constants for *Fm*3*m*-LaX (X = P, As) are basically consistent with the previous theoretical values.[9,42,43] For *P*4/*mmm*-LaX (X = P, As), the values of C_{11} and C_{33} are similar, indicating that they have an almost isotropic linear incompressibility. For the higher-pressure phases *C*2/*m*-LaP and *Imma*-LaAs, their elastic constants (C_{11}, C_{22} and C_{33}) are larger than those of other phases, suggesting that they are more difficult to compress.

In addition to checking the mechanical stability, the elastic properties can also be used to explain various phenomena, such as inter-atomic potentials, phonon spectra, specific and thermal expansion.[44] Table 3 gives the results of bulk modulus *B* (GPa), shear modulus *G* (GPa), *G*/*B* ratio, Young's modulus *E* (GPa), Poisson's ratio and Vickers hardness H_v (GPa) of LaX (X = P, As). It can be seen that *C*2/*m*-LaP and *Imma*-LaAs possess the larger values of bulk, shear and Young's modulus, implying the potential hard properties. Our results show that *P*4/*mmm*-LaP and *P*4/*mmm*-LaAs exhibit ductility, and others are brittle. The type of the bonding can be measured by Poisson ratio (the threshold value of Poisson's ratio is 0.25,[45] the covalent bonding ($\nu < 0.25$) corresponds to ionic materials and the ionic bonding ($\nu \geq 0.25$) corresponds to ionic materials. The Poisson's ratios of *P*4/*mmm*-LaX (X = P, As) and *Imma*-LaAs are larger than 0.25, suggesting that they are ionic crystals and the ionic bond component is dominant. While for the Poisson's ratio of *C*2/*m*-LaP, its small value implies that there are a lot of strong covalent bonds.

The hardness can be estimated by Vickers hardness H_v proposed by Chen *et al.*[46] This empirical model is expressed as $H_v = 2(k^2G)^{0.585} - 3$ (where H_v is the Vickers hardness, *G* is the shear modulus, and *k* is the value of *G*/*B*), which has been successfully applied to a wide range of material systems.[47–51] For *C*2/*m*-LaP and *Imma*-LaAs, the hardness values are 23.24 GPa and 19.24 GPa, respectively. The hardness are much higher than

Table 3 Bulk modulus *B* (GPa), shear modulus *G* (GPa), *G*/*B* ratios, Young's modulus *E* (GPa), Poisson's ratios ν and Vickers hardness H_v (GPa) of LaX (X = P, As) at different pressures

LaP	*B* (GPa)	*G* (GPa)	*G*/*B*	*E* (GPa)	ν	H_v (GPa)
*Fm*3*m*	72.26	44.59	0.62	110.95	0.244	7.48
*P*4/*mmm*	241.51	111.61	0.46	290.00	0.289	9.79
*C*2/*m*	323.69	204.38	0.63	506.53	0.239	23.24
LaAs	*B* (GPa)	*G* (GPa)	*G*/*B*	*E* (GPa)	ν	H_v (GPa)
*Fm*3*m*	70.11	42.24	0.60	105.53	0.249	6.88
*P*4/*mmm*	241.43	107.23	0.44	279.95	0.292	8.92
Imma	324.10	186.17	0.57	468.76	0.259	19.24

Table 2 Calculated elastic constants (GPa) of LaX (X = P, As) at different pressures

	LaP			LaAs		
	*Fm*3*m* (0 GPa)	*P*4/*mmm* (50 GPa)	*C*2/*m* (100 GPa)	*Fm*3*m* (0 GPa)	*P*4/*mmm* (50 GPa)	*Imma* (100 GPa)
C_{11}	162.02	355.55	640.99	164.64	340.87	602.52
C_{22}			646.96			452.63
C_{33}		381.12	444.72		392.67	595.21
C_{44}	33.65	105.32	373.69	29.46	100.68	232.98
C_{55}			162.44			165.22
C_{66}		199.68	251.30		207.64	308.71
C_{12}	27.39	225.75	112.16	22.84	230.87	359.86
C_{13}		158.09	199.50		159.31	124.87
C_{23}			286.86			162.29
C_{14}						
C_{15}			48.81			
C_{25}			−77.01			
C_{35}			35.48			
C_{46}			−53.87			

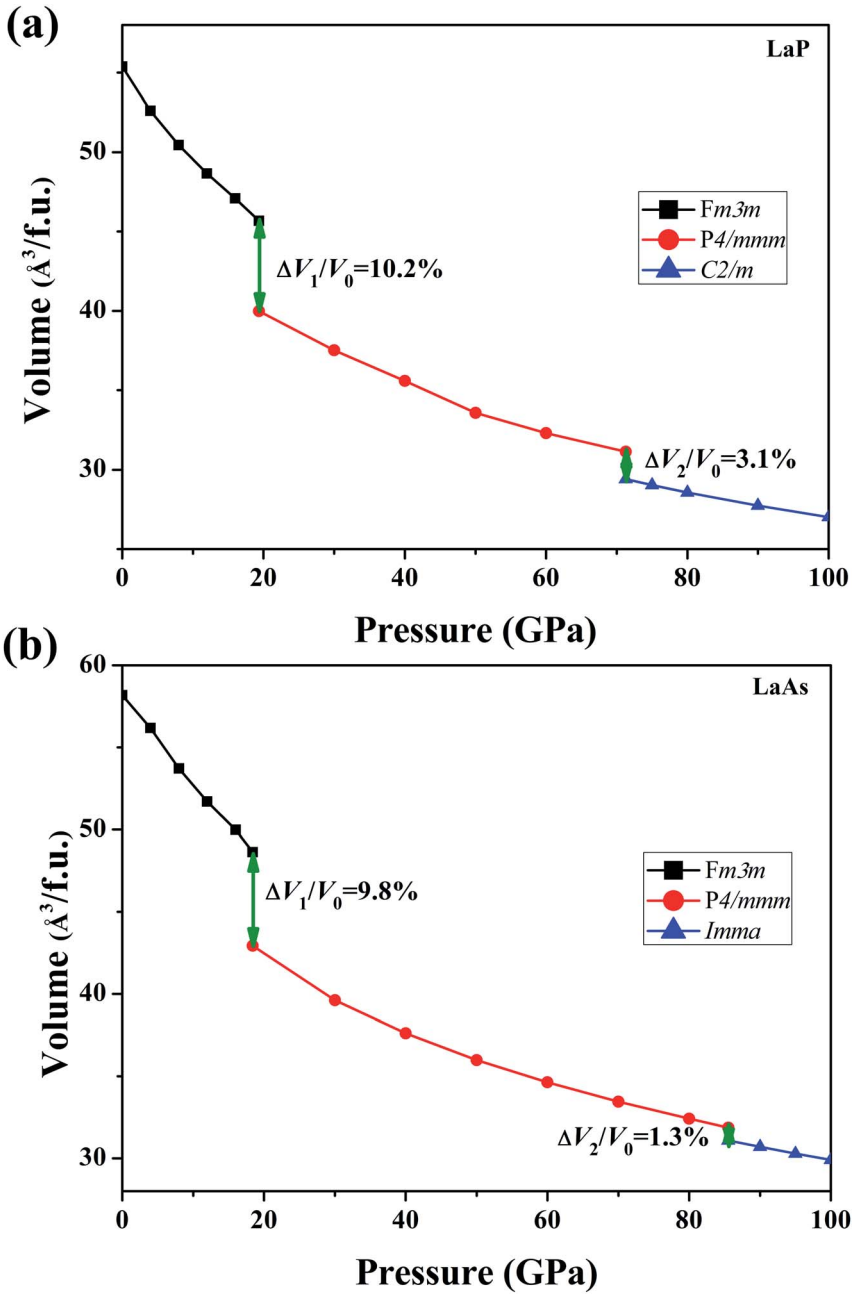

Fig. 3 Calculated volumes as a function of pressure for (a) LaP and (b) LaAs, where V_0 represents the equilibrium volume of *Fm*3*m*-LaX (X = P, As).

those of other phases. Especially for *C*2/*m*-LaP phase whose hardness is similar to those of ReB_2 (ref. [52]) and WB_2,[27] indicating that it is a potential hard material.

For engineering materials, elastic anisotropy is an important factor affecting their applications. Fig. 4 shows the direction dependence of the Young's modulus for LaX (X = P, As) and the corresponding slice in the *xy*, *yz*, *xz* planes. The cubic phases of LaP and LaAs exhibit the isotropic Young's modulus. It can be seen that the anisotropy of Young's modulus of LaP-*P*4/*mmm* and LaAs-*P*4/*mmm* is basically the same. Structural anisotropy can cause the orientation difference of these compounds. The maximum values of Young's modulus are 625 GPa along *xy* plane for *C*2/*m*-LaP and 536 GPa along *yz* plane for *Imma*-LaAs. Accordingly, their minimum values are 388 GPa and 312 GPa, respectively. The ratios of E_{max}/E_{min} are 1.61 and 1.72, respectively, indicating the comparable anisotropy of Young's modulus.

3.3 Lattice dynamic properties

To confirm their dynamical stabilities, we calculated a series of phonon dispersion curves of stable structures at different pressures. Through our previous researches,[38,39] it has been

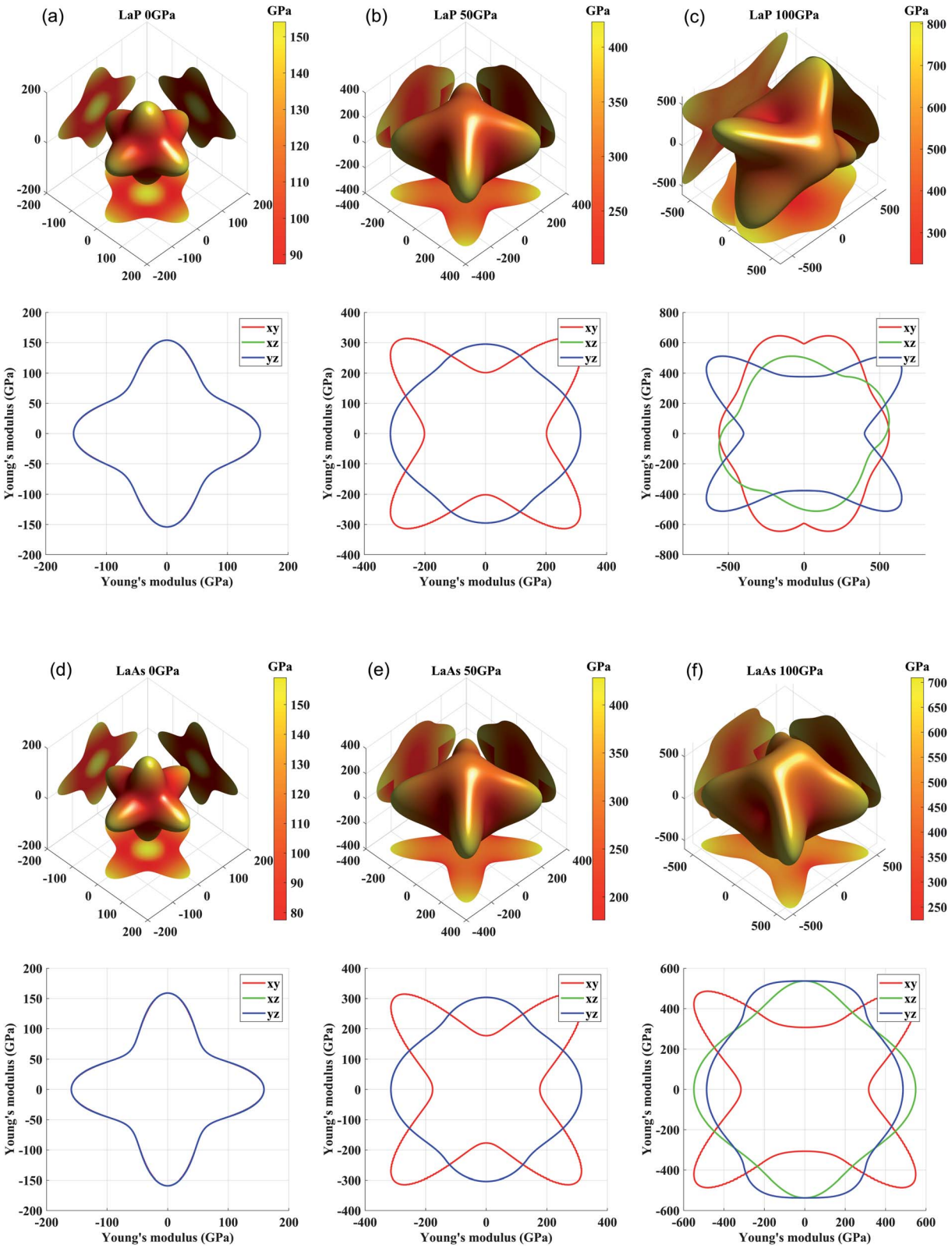

Fig. 4 Three-dimensional and two-dimensional surface representations of Young's modulus for (a) LaP-*Fm*3*m*, (b) LaP-*P*4/*mmm*, (c) LaP-*C*2/*m*, (d) LaAs-*Fm*3*m*, (e) LaAs-*P*4/*mmm*, and (f) LaAs-*Imma*.

proved that *Fm*3*m*-LaP and *Fm*3*m*-LaAs are stable at 0 GPa, and the phonon spectra have no imaginary frequency. The phonon spectra of the *P*4/*mmm*-LaP and *P*4/*mmm*-LaAs at 50 GPa and *C*2/*m*-LaP and *Imma*-LaAs at 100 GPa are shown in Fig. 5. There are no imaginary phonon frequencies in the all considered structures, indicating these phases are all dynamically stable.

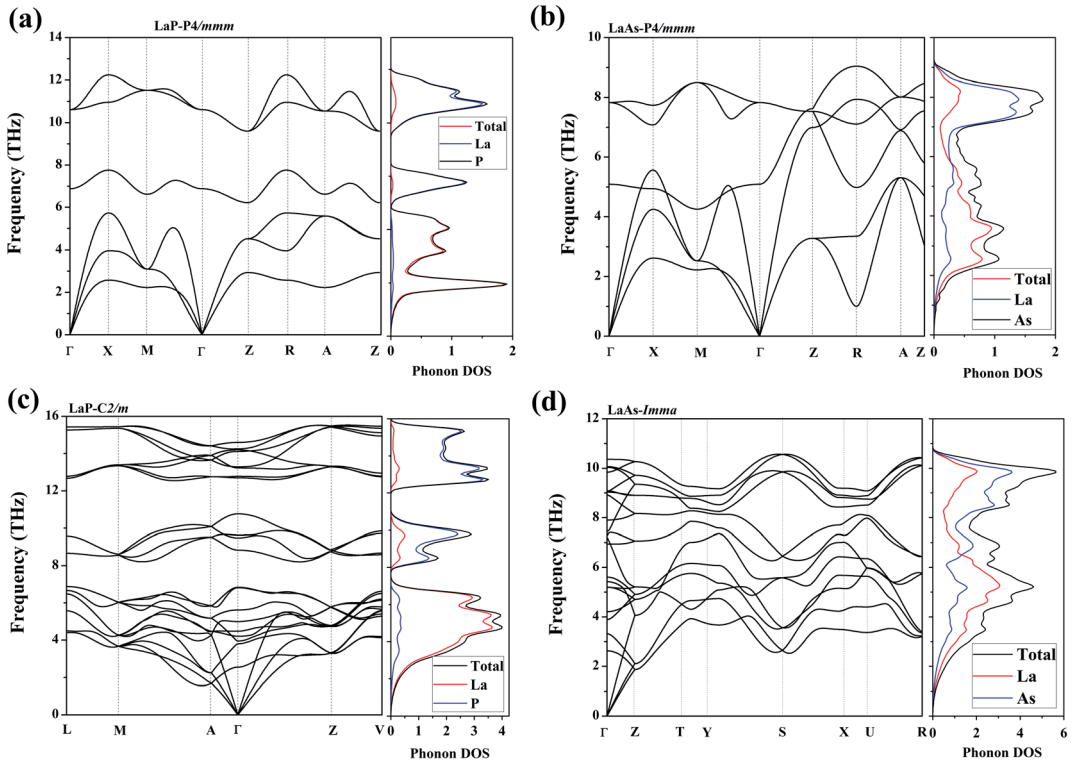

Fig. 5 Phonon dispersions and the total and partial phonon density of states (DOSs) for (a) LaP-*P*4/*mmm*, (b) LaAs-*P*4/*mmm*, (c) LaP-*C*2/*m* and (d) LaAs-*Imma*.

Because of the structural similarity of LaP and LaAs at 50 GPa, their phonon spectra are generally similar. However, due to the different atomic weights of La and P atoms, there are phonon gaps in the phonon spectra of LaP. It can be seen from the phonon DOS that the vibrations of La and P are completely decoupled in *P*4/*mmm*-LaP and *C*2/*m*-LaP, and the main contribution of acoustic branches comes from La atoms, while the high-frequency branches mainly correspond to the P/As atoms.

Phonon velocities are closely related to the phonon transportation, the phonon velocities of LaX (X = P, As) at different pressures are obtained from the phonon dispersions. The two phonon velocities (v_p is the phase velocity and v_g is the group velocity) are defined as:[53,54] $v_p = \omega(k)/k, v_g = \nabla_k\omega(k)$, where k is the distance between two points in the Brillouin zone, $\omega(k)$ is the dispersion relation. Considering the anisotropy of *P*4/*mmm*-LaP and *P*4/*mmm*-LaAs, Fig. 6a–d shows the phonon phase velocities and group velocities along [100] and [001] directions. As we can see, the phase velocities of optical branches are much larger than those of acoustic modes, but in contrast, the group velocities of acoustic branches are about three times as large as those of optical branches. This phenomenon can also be found in the phonon velocities of *C*2/*m*-LaP and *Imma*-LaAs, as shown in the Fig. 6e and f. These results can be understood from the equations of phase velocity and group velocity. The phase velocity is directly proportional to the phonon frequency, and the phase velocities of the optical branches are larger than those of the acoustic branches because of their larger phonon frequencies. While the group velocities are obtained from the slope of the phonon dispersion, and the acoustic branches are steeper near the Γ point, so their group velocities are larger than those of the optical branches.

Fig. 7 shows the atomic displacements of LaP and LaAs at different pressures. The displacements of La and P/As atoms are indicated by yellow and grey arrows, respectively. For *P*4/*mmm*-LaP/LaAs, the vibration direction of La atom is opposite to that of P/As atoms. For *Imma*-LaAs, the structure is a layered along the *c* direction. The two adjacent layers are composed of the same atoms, forming a folded layered structure. The vibration directions of different atoms in each layer are opposite. The most intricate one is LaP-*C*2/*m*, similar to the combination of two interactive vibrations. We assume that the primitive cell is divided into left and right parts along the *b* axis, and the vibration direction of different atoms in each part is different.

3.4 Electronic structure

Electronic properties play a key role in the study of other properties of solid materials.[55–57] Fig. 8 presents the density of state (DOS) over their stable pressure ranges. From the calculated DOS curves, we can see that *P*4/*mmm*-LaX (X = P, As), *C*2/*m*-LaP and *Imma*-LaAs all exhibit metallic characteristics, confirmed by the non-zero electronic DOS at the Fermi level. It is obvious that the DOS near Fermi level is mainly composed of La-d states mixed with La-f and P/As-p, while the contributions of La-p and P/As-s states are mainly located far away from the Fermi level. For *P*4/*mmm*-LaX (X = P, As) structures, it is notable

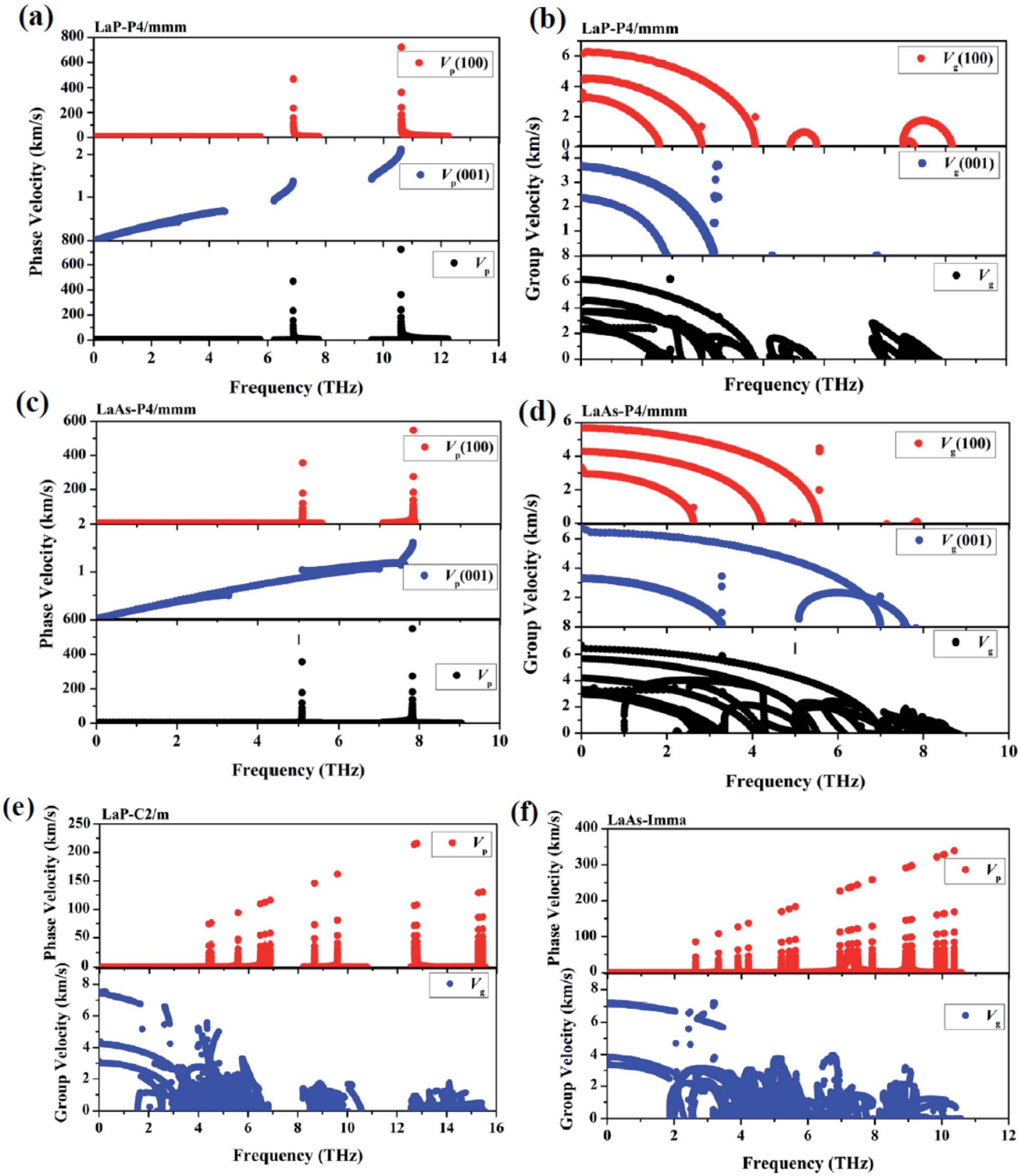

Fig. 6 The calculated phonon phase velocities and group velocities of LaP-*P*4/*mmm* (a) and (b), LaAs-*P*4/*mmm* (c) and (d), LaP-*C*2/*m* (e) and LaAs-*Imma* (f).

that P/As-p orbital is the main supplier in the energy range of −7–0 eV, while from 0–3 eV, the DOS is mainly dominated by the La-d orbital. The allopatric distribution of P/As-p and La-d may be responsible for the lower hardness of the two tetragonal phases. For *C*2/*m*-LaP, the peaks of La-d/f and P-p orbitals overlap from −3–3 eV, indicating that there is strong hybridization between La and P atoms, which is regarded as covalent bonds nature. While for *Imma*-LaAs, the peaks overlap becomes fewer, which means that the covalent bond becomes weaker.

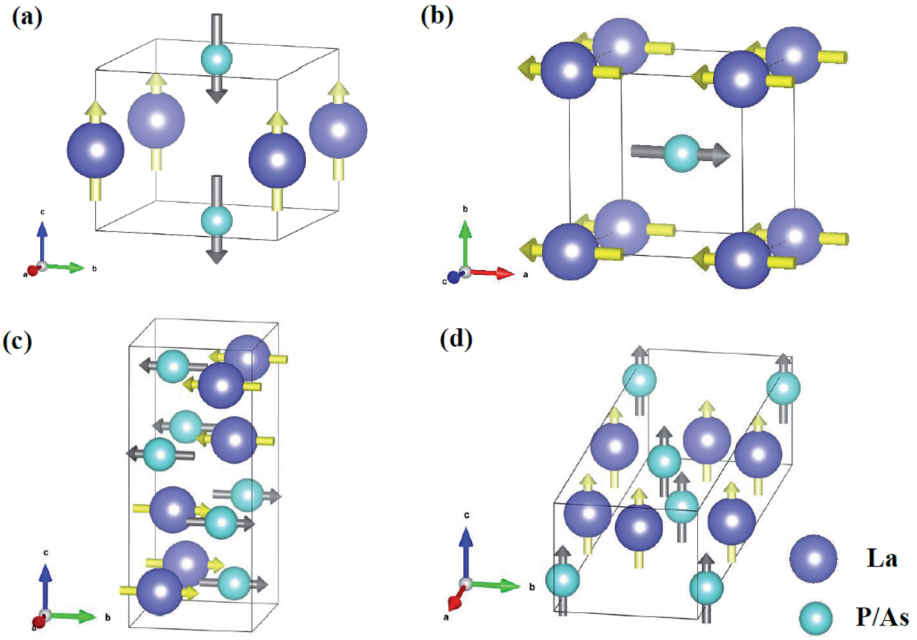

Fig. 7 Main atomic displacements of (a) *P*4/*mmm*-LaP, (b) *P*4/*mmm*-LaAs, (c) LaP-*C*2/*m* and (d) LaAs-*Imma*. The displacements of La and P/As atoms are indicated by yellow and grey arrows, respectively.

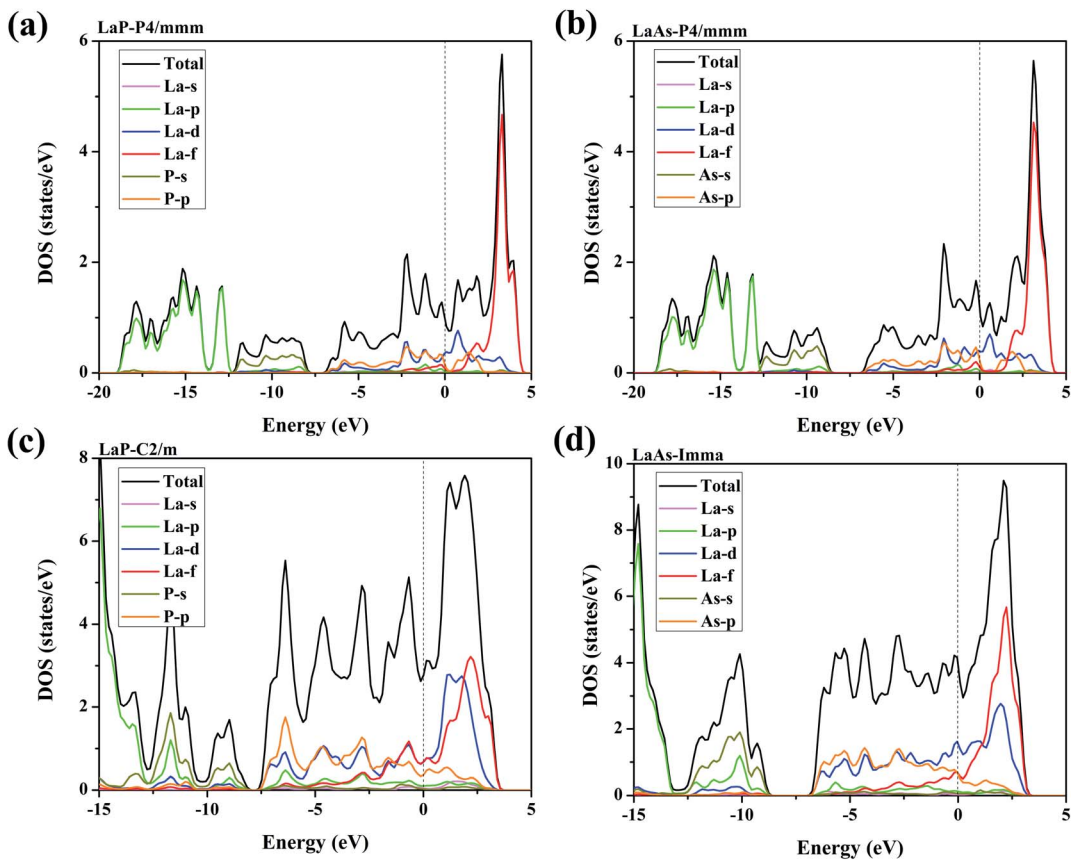

Fig. 8 Calculated total and projected DOS for (a) LaP-*P*4/*mmm*, (b) LaAs-*P*4/*mmm*, (c) LaP-*C*2/*m* and (d) LaAs-*Imma*. The vertical dash lines represent the Fermi level.

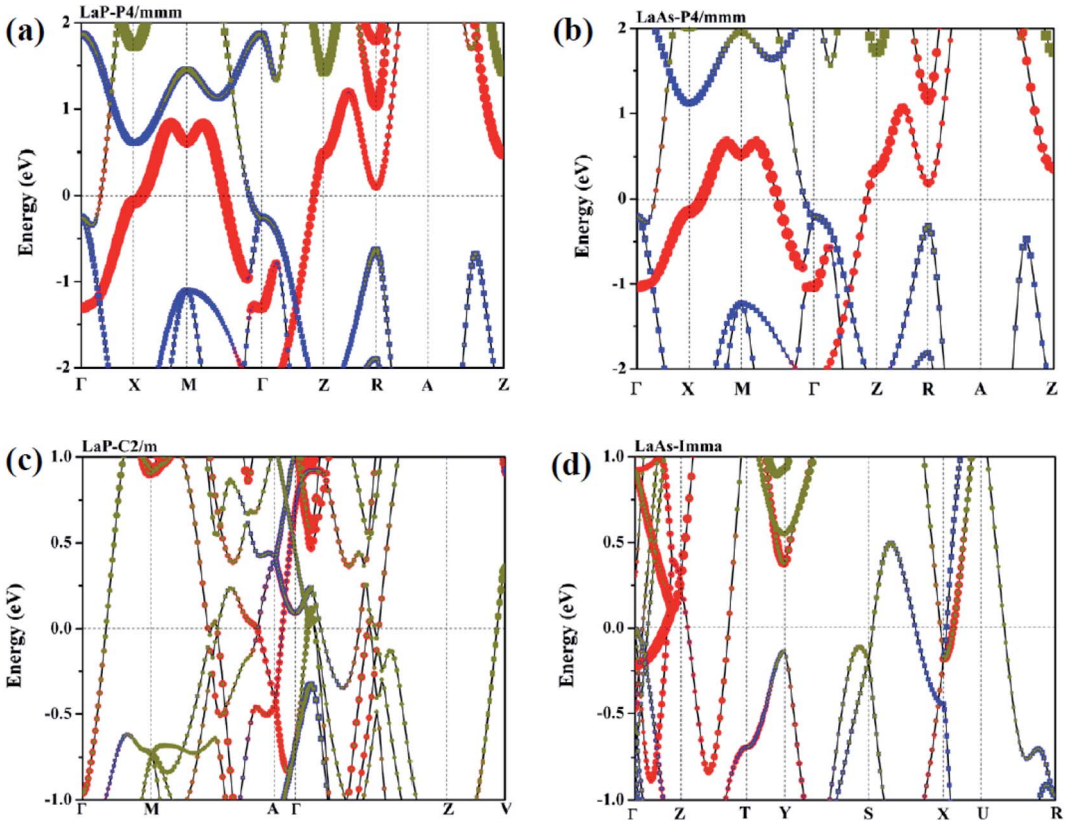

Fig. 9 Calculated projected band structures for (a) LaP-*P*4/*mmm*, (b) LaAs-*P*4/*mmm*, (c) LaP-*C*2/*m* and (d) LaAs-*Imma*. The red and yellow bubbles represent the contributions of La-d and La-f orbitals. The blue squares represent the contributions of P/As-p orbitals.

In order to further explore the contribution of each orbit near Fermi level, Fig. 9 presents the projected band structures of LaX with the spectral weight of La-f, La-d orbitals and P/As-p orbitals. The results also demonstrate the metallic characteristics of these high-pressure structures due to the absence of the band gap at the Fermi level. The observation of the projected band structures shows that *P*4/*mmm*-LaP and *P*4/*mmm*-LaAs have similar electronic distributions near Fermi level, which is in good agreement with the results of density of state (DOS). The valence band is mainly composed of mixed states of P/As-p and La-d states, while the conduction band is mainly composed of La-d states with a significant contribution from La-f and P/As-p states. For the *C*2/*m*-LaP and *Imma*-LaAs, their band structures remain metallic; however, the contributions of La-f orbitals near the Fermi surface are larger than those of *P*4/*mmm*-LaP and *P*4/*mmm*-LaAs.

To further study the chemical bonds properties of the La–P/As combinations, the electronic localization function (ELF) of LaX (X = P, As) are calculated as depicted in Fig. 10, which can imply the localizing degree of electrons in the certain regions.[58] ELF values can provide useful information about the chemical bonding properties by qualitatively defining the bonding nature

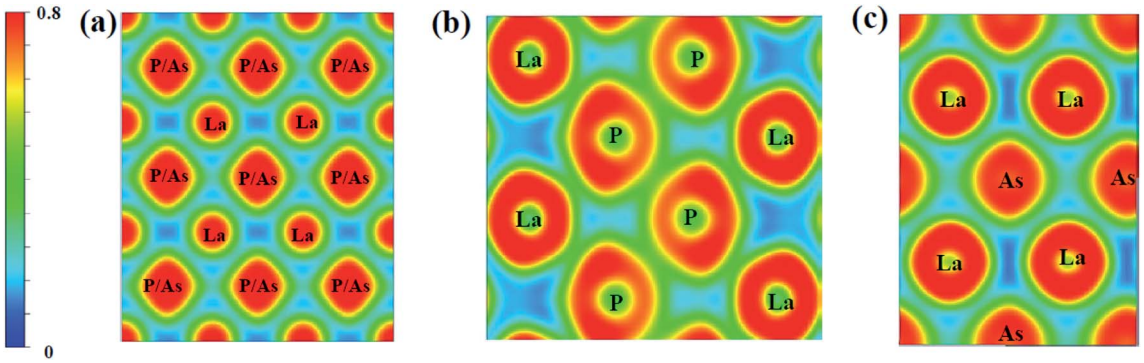

Fig. 10 Electron localization function of LaX (X = P, As) in (100) plane at different pressures: (a) LaP-*P*4/*mmm* and LaAs-*P*4/*mmm* at 50 GPa, (b) LaP-*C*2/*m* at 100 GPa, (c) LaAs-*Imma* at 100 GPa, respectively.

to iconicity, covalency or metallicity.[44] The localizing degree of electrons in the related regions gradually increases from 0 to 1. It can be seen that the electronic localization function of *P*4/*mmm*-LaX (X = P, As) gradually changes between La and As/P atoms, which means there exist P–P covalent bonds and La–P ionic bonds. In the Fig. 10b and c, the electronic localization function for *C*2/*m*-LaP and *Imma*-LaAs are similar, while the overlap of electronic localization function for La–P and P–P atoms in *C*2/*m*-LaP is much larger in *Imma*-LaAs. This indicates the La–P ionic bonds and P–P covalent bonds in LaP-*C*2/*m* are stronger, that is to say, *C*2/*m*-LaP has larger bonding strength, so the hardness is higher than other phases. The results of electronic localization function of each phase of LaX are consistent with the analysis of density of states. The bonding strength and the proportion of the covalent play a key role in the incompressibility and hardness of the compounds.

4. Conclusions

In summary, the CALYPSO is used to search the possible structures of LaX (X = P, As) under pressures up to 100 GPa. We have predicted two novel high-pressure phases of lanthanide phosphates LaP and LaAs in the pressure range of 0–100 GPa. The phase transition, mechanical, thermodynamic properties, and electronic structures of these compounds are further studied by first principles. The predicted phase transition sequence of LaP is $Fm3m \rightarrow P4/mmm \rightarrow C2/m$ with transition pressures of 19.04 GPa and 70.08 GPa, and the phase transition sequence of LaAs is $Fm3m \rightarrow P4/mmm \rightarrow Imma$ with transition pressures of 17.22 GPa and 85.53 GPa. The calculations of phonon dispersions, elastic constants and formation enthalpies showed that these phases are stable. According to the elastic properties, we have evaluated the hardness values of *C*2/*m*-LaP and *Imma*-LaAs are 23.24 and 19.24 GPa, respectively, indicating that they are potential hard materials. In addition, the electronic properties of these compounds at dominating pressures are also investigated to explore the intrinsic chemical bonding characteristics and to find out the reason for their higher hardness. These results are of great significance for further understanding of the high-pressure characteristics of the rare earth phosphates and for providing guidance of the applications in modern industry.

Conflicts of interest

There are no conflicts to declare.

Acknowledgements

This work was supported by the National Natural Science Foundation of China (Grant No. 12074274), the NSAF (Grant No. U1830101), and the Science Challenge Project (Grant No. TZ2016001). We also acknowledge the support for the computational resources by the State Key Laboratory of Polymer Materials Engineering of China in Sichuan University.

References

1 G. A. Prinz, *Science*, 1999, **283**, 330.
2 S. S. Sun, Q. Wang, P. J. Guo, K. Liu and H. C. Lei, *New J. Phys.*, 2016, **18**, 082002.
3 M. Zhang, X. Q. Wang, A. Rahman, R. C. Dai, Z. P. Wang and Z. M. Zhang, *Phys. Rev. B*, 2020, **101**, 064106.
4 S. Khalid, A. Sharan and A. Janotti, *Phys. Rev. B*, 2020, **101**, 125105.
5 Y. Wu, T. Kong, L. L. Wang, D. D. Johnson, D. X. Mou, L. N. Huang, B. Schrunk, S. L. Bud'ko, P. C. Canfield and A. Kaminski, *Phys. Rev. B*, 2016, **94**, 081108.
6 L. Petit, Z. Szotek, M. Luders and A. Svane, *J. Phys.: Condens. Matter*, 2016, **28**, 223001.
7 H. Y. Yang, T. Nummy, H. Li, S. Jaszewski, M. Abramchuk, D. S. Dessau and F. Tafti, *Phys. Rev. B*, 2017, **96**, 235128.
8 F. F. Tafti, Q. D. Gibson, S. K. Kushwaha, N. Haldolaarachchige and R. J. Cava, *Nat. Phys.*, 2016, **12**, 272–277.
9 M. Shoaib, G. Murtaza, R. Khenata, M. Farooq and R. Ali, *Comput. Mater. Sci.*, 2013, **79**, 239–246.
10 A. Svane, V. Kanchana, G. Vaitheeswaran, G. Santi, W. M. Temmerman, Z. Szotek, P. Strange and L. Petit, *Phys. Rev. B: Condens. Matter Mater. Phys.*, 2005, **71**.
11 F. Hulliger and H. R. Ott, *J. Less-Common Met.*, 1977, **55**, 103–113.
12 Z. Charifi, A. H. Reshak and H. Baaziz, *Solid State Commun.*, 2008, **148**, 139–144.
13 G. Vaitheeswaran, V. Kanchana and M. Rajagopalan, *Phys. B*, 2002, **315**, 64–73.
14 Y. S. Kwon, M. Takeshige, T. Suzuki and T. Kasuya, *Phys. B*, 1990, **163**, 328–330.
15 H. M. Tütüncü, S. Bagci and G. P. Srivastava, *J. Phys. Condens. Matter*, 2007, **19**, 156207.
16 T. Adachi, I. Shirotani, J. Hayashi and O. Shimomura, *Phys. Lett. A*, 1998, **250**, 389–393.
17 A. Hasegawa, *J. Phys. Soc. Jpn.*, 1985, **54**, 677–684.
18 Y. Kaneta, O. Sakai and T. Kasuya, *Phys. B*, 1993, **186–88**, 156–158.
19 I. Shirotani, K. Yamanashi, J. Hayashi, N. Ishimatsu, O. Shimomura and T. Kikegawa, *Solid State Commun.*, 2003, **127**, 573–576.
20 G. Vaitheeswaran, V. Kanchana and M. Rajagopalan, *J. Alloys Compd.*, 2002, **336**, 46–55.
21 I. Shirotani, K. Yamanashi, J. Hayashi, Y. Tanaka, N. Ishimatsu, O. Shimomura and T. Kikegawa, *J. Phys.: Condens. Matter*, 2001, **13**, 1939–1946.
22 G. Vaitheeswaran, L. Petit, A. Svane, V. Kanchana and M. Rajagopalan, *J. Phys.: Condens. Matter*, 2004, **16**, 4429–4440.
23 Y. C. Wang, J. A. Lv, L. Zhu and Y. M. Ma, *Phys. Rev. B: Condens. Matter Mater. Phys.*, 2010, **82**, 094116.
24 Y. C. Wang, J. Lv, L. Zhu and Y. M. Ma, *Comput. Phys. Commun.*, 2012, **183**, 2063–2070.
25 Y. M. Chen, H. Y. Geng, X. Z. Yan, Y. Sun, Q. Wu and X. R. Chen, *Inorg. Chem.*, 2017, **56**, 3867–3874.

26 J. J. Wang, G. L. Sun, P. L. Kong, W. G. Sun, C. Lu, F. Peng and X. Y. Kuang, *Phys. Chem. Chem. Phys.*, 2017, **19**, 16206–16212.
27 H. Y. Zhang, F. Xi, Z. Y. Zeng, X. R. Chen and L. C. Cai, *J. Phys. Chem. C*, 2017, **121**, 7397–7403.
28 C. Z. Zhang, G. L. Sun, J. J. Wang, C. Lu, Y. Y. Jin, X. Y. Kuang and A. Hermann, *ACS Appl. Mater. Interfaces*, 2017, **9**, 26169–26176.
29 J. P. Perdew, J. A. Chevary, S. H. Vosko, K. A. Jackson, M. R. Pederson, D. J. Singh and C. Fiolhais, *Phys. Rev. B: Condens. Matter Mater. Phys.*, 1992, **46**, 6671–6687.
30 P. E. Blochl, *Phys. Rev. B: Condens. Matter Mater. Phys.*, 1994, **50**, 17953–17979.
31 G. Kresse and J. Furthmuller, *Phys. Rev. B: Condens. Matter Mater. Phys.*, 1996, **54**, 11169–11186.
32 X. Gonze and C. Lee, *Phys. Rev. B: Condens. Matter Mater. Phys.*, 1997, **55**, 10355–10368.
33 A. Togo and I. Tanaka, *Scr. Mater.*, 2015, **108**, 1–5.
34 A. Savin, O. Jepsen, J. Flad, O. K. Andersen, H. Preuss and H. G. Vonschnering, *Angew. Chem., Int. Ed.*, 1992, **31**, 187–188.
35 A. D. Becke and K. E. Edgecombe, *J. Chem. Phys.*, 1990, **92**, 5397–5403.
36 X. Z. Yan, Y. M. Chen, X. Y. Kuang and S. K. Xiang, *J. Appl. Phys.*, 2014, **116**, 083707.
37 A. H. Reshak, Z. Charifi and H. Baaziz, *J. Phys.: Condens. Matter*, 2008, **20**, 325207.
38 Y. Zhou, Y. Cheng, X. R. Chen, C. E. Hu and Q. F. Chen, *Philos. Mag.*, 2018, **98**, 1900–1918.
39 Y. Zhou, W. L. Tao, Z. Y. Zeng, X. R. Chen and Q. F. Chen, *J. Appl. Phys.*, 2019, **125**, 045107.
40 F. Mouhat and F. X. Coudert, *Phys. Rev. B: Condens. Matter Mater. Phys.*, 2014, **90**, 224104.
41 Z. J. Wu, E. J. Zhao, H. P. Xiang, X. F. Hao, X. J. Liu and J. Meng, *Phys. Rev. B: Condens. Matter Mater. Phys.*, 2007, **76**, 054115.
42 E. Deligoz, K. Colakoglu, Y. O. Ciftci and H. Ozisik, *J. Phys.: Condens. Matter*, 2007, **19**, 436204.
43 G. Pagare, S. P. Sanyal and P. K. Jha, *J. Alloys Compd.*, 2005, **398**, 16–20.
44 L. Chen, J. L. Xu, M. G. Zhang, Z. R. Wen and Z. Y. Jiang, *J. Alloys Compd.*, 2020, **813**, 152246.
45 J. Haines, J. M. Leger and G. Bocquillon, *Annu. Rev. Mater. Res.*, 2001, **31**, 1–23.
46 X. Q. Chen, H. Y. Niu, D. Z. Li and Y. Y. Li, *Intermetallics*, 2011, **19**, 1275–1281.
47 A. Misra and W. Y. Ching, *Sci. Rep.*, 2013, **3**, 1488.
48 X. Q. Chen, H. Y. Niu, C. Franchini, D. A. Z. Li and Y. Y. Li, *Phys. Rev. B: Condens. Matter Mater. Phys.*, 2011, **84**, 121405.
49 H. Y. Gou, Z. P. Li, L. M. Wang, J. Lian and Y. C. Wang, *AIP Adv.*, 2012, **2**, 012171.
50 Y. C. Liang, Y. P. Gou, X. Yuan, Z. Zhong and W. Q. Zhang, *Chem. Phys. Lett.*, 2013, **580**, 48–52.
51 M. G. Zhang, H. Y. Yan and Q. Wei, *J. Alloys Compd.*, 2019, **774**, 918–925.
52 X. F. Hao, Y. H. Xu, Z. J. Wu, D. F. Zhou, X. J. Liu, X. Q. Cao and J. Meng, *Phys. Rev. B: Condens. Matter Mater. Phys.*, 2006, **74**, 224112.
53 Y. C. Ding and B. Xiao, *RSC Adv.*, 2015, **5**, 18391–18400.
54 X. Feng, J. W. Xiao, R. Melnik, Y. Kawazoe and B. Wen, *J. Chem. Phys.*, 2015, **143**, 104503.
55 M. H. Zhang, X. L. Chen, W. X. Ji, P. J. Wang, Y. Min and C. W. Zhang, *Appl. Phys. Lett.*, 2020, **116**, 172105.
56 A. N. Ma, S. S. Li, S. F. Zhang, C. W. Zhang, W. X. Ji, P. Li and P. J. Wang, *Phys. Chem. Chem. Phys.*, 2019, **21**, 5165–5169.
57 S. Q. Feng, Y. Yang, F. Guo, L. Su, X. R. Cheng, C. S. Yuan and K. Yang, *J. Alloys Compd.*, 2020, **844**, 156098.
58 B. Silvi and A. Savin, *Nature*, 1994, **371**, 683–686.